Multidimensional fractal scaling analysis using higher order moving average polynomials and its fast algorithm

Hanqiu Ju [a], Naoki Honda [a,c,d,e], Shige H. Yoshimura [f], Miki Kaneko [b], Taiki Shigematsu [b], Ken Kiyono [b,*]

[a] *Laboratory of Theoretical Biology, Graduate School of Biostudies, Kyoto University, Yoshidakonoecho, Sakyo, Syoto 606-8315, Japan*
[b] *Graduate School of Engineering Science, Osaka University, 1-3 Machikaneyama-cho, Toyonaka, Osaka 560-8531, Japan*
[c] *Laboratory of Data-driven Biology, Graduate School of Integrated Sciences for Life, Hiroshima University, Kagamiyama, Higashi-Hiroshima, Hiroshima 739-8526, Japan*
[d] *Kansei-Brain Informatics Group, Center for Brain, Mind and Kansei Sciences Research (BMK Center), Hiroshima University, Kasumi, Minami-ku, Hiroshima 734-8551, Japan*
[e] *Theoretical Biology Research Group, Exploratory Research Center on Life and Living Systems (ExCELLS), National Institutes of Natural Sciences, Okazaki, Aichi, Japan*
[f] *Laboratory of Plasma Membrane and Nuclear Signaling, Graduate School of Biostudies, Kyoto University, Kyoto, Japan*

ARTICLE INFO

ABSTRACT

The detrending moving average (DMA) analysis demonstrates excellent performance for the characterization of long-range correlations and fractal scaling and is performed in various research fields. The conventional DMA with a simple moving average can remove linear trends embedded in the observed time series. To improve the detrending ability of the DMA, higher-order DMA including a higher order polynomial detrending was also introduced using the Savitzky-Golay filter and its fast implementation algorithm was developed. However, the higher-order DMA applicable to higher dimensional data is yet to be well established. As the data dimension increases, an increase in the computational cost becomes a problem that needs to be resolved. Further, the implementation of the higher order DMA is a time-consuming procedure. To resolve this problem, we here proposed a fast algorithm for multidimensional DMA with higher order polynomial detrending. In the proposed algorithm, to reduce the computational complexity, parallel translation and recurrence techniques are introduced. Monte Carlo experiments for two-dimensional data show that the computational time of the proposed algorithm is approximately proportional to the cubic of the data length, whereas the computational time of the conventional implementation is approximately proportional to the quartic of the data length. Moreover, we evaluate the estimation accuracy of the Hurst exponent of the proposed method. Finally, we demonstrate the possible application of the proposed method by estimating the Hurst exponent of images.

1. Introduction

Long-range correlation and fractal scaling behavior are omnipresent in various systems, e.g., biological [1–4], economic [5–7], and social systems [8,9]. To characterize such phenomena, various scaling exponents have been proposed. For instance, the Hurst exponent H is the parameter of fractional Brownian motion (fBm) [10] with long-range correlated increments and is defined based on the self-affine structure of the fBm. H has been proven useful in characterizing one-dimensional and higher dimensional data. For example, in the one-dimensional case, the long-term heart-rate variability (HRV) time series exhibiting a $1/f^\beta$-type power spectrum [11,12] can be characterized by H. The power-law exponent β is also the scaling exponent and is linked with H as $\beta = 2H + 1$ ($\beta > 1$) [13]. In higher dimensional cases, H-based fractal concepts are used to model and quantify isotropic and anisotropic fracture surfaces [14,15].

To characterize fractal scaling behavior in one-dimensional and higher dimensional cases, power spectral analysis method [16,17], wavelet-transform-based analysis method [18–21], detrended fluctuation analysis (DFA) [2,22], and detrending moving average

(DMA) algorithms [6,23] have been proposed. Among these methods, DMA is one of the best methods to estimate H owing to its accurate result and the easy implementation. However, the detrending ability of DMA is worse than higher order DFA because the trend is estimated by simple moving average. This lack of detrending ability will affect the reliability of the estimated result and cause the spurious detection of H.

Higher order DMA, which is based on higher order moving average polynomials, was proposed to improve the detrending capability [24]. This higher order approach shows better detrending capability in terms of removing a higher order polynomial trend [25]. Moreover, it has been confirmed that higher order DMA exhibits better performance while performing long-range correlation and characterizing fractal scaling behavior owing to its detrending ability and stabilities, whereas the nonlinear filtering property of DFA results in the instability of the scaling exponent estimation [25,26]. However, such higher order DMA has just been established in one-dimensional space, and the higher dimensional implementation of higher order DMA has not been established. Moreover, a fast algorithm for one-dimensional higher order DMA has been developed because the conventional implementation of DMA based on the convolutional operation is time-consuming [13]. As data dimensions increase, the computational cost increases, and thus, there is a demand for the development of fast algorithms.

In this study, we propose a multidimensional higher order detrending moving average approach to estimate the scaling exponent corresponding to H. First, we introduce the general description of multidimensional DMA; next, we derive the second-order and fourth-order DMA in 2D space. To reduce the computational time, we propose their fast algorithms. To evaluate the accuracy of our algorithm, we test our algorithm numerically with different data sizes and H values. Moreover, we discuss the applicability of the proposed method to biological image analysis to characterize the actin filament network behind the cell cortex. In the appendices, we demonstrate the detectable scaling exponent and detrending capability for removing the polynomial trend to show the efficiency of the proposed method.

2. Multidimensional scaling analysis using a higher order moving polynomial function

2.1. Multidimensional scaling analysis using moving average

In this subsection, we review the multidimensional detrending moving average method. To analyze high-dimensional fractals, a generalized multidimensional detrending moving average method has been proposed [23]. In d-dimensional space, the scale can be represented by a subarray $\mathbf{n} = (n_1, n_2, \ldots, n_d)$. If we choose $n_1 = n_2 = \cdots = n_d = s$ ($s > 1$ is an odd positive integer), the generalized variance at scale s is defined as:

$$\sigma^2_{\text{DMA}}(s) = \frac{1}{\prod_{i=1}^{d}(N_i - s + 1)} \sum_{x_1=(s-1)/2}^{N_1-(s-1)/2} \cdots \sum_{x_d=(s-1)/2}^{N_d-(s-1)/2} \left[f(\mathbf{x}_d) - \tilde{f}(\mathbf{x}_d) \right]^2. \quad (1)$$

where $\mathbf{x}_d = (x_1, x_2, \ldots, x_d)$ and $f(\mathbf{x}_d)$ denotes the d-dimensional data, e.g., an fBm surface, and N_i denotes the length of x_i in the ith dimension. $\tilde{f}(\mathbf{x}_d)$ is the moving average function of $f(\mathbf{x}_d)$, which is defined by:

$$\tilde{f}(x_1, \ldots, x_d) = \frac{1}{s^d} \sum_{\xi_1=-(s-1)/2}^{(s-1)/2} \cdots \sum_{\xi_d=-(s-1)/2}^{(s-1)/2} f(x_1 + \xi_1, \ldots, x_d + \xi_d). \quad (2)$$

If $f(x_1, x_2, \ldots, x_d)$ has an fBm-surface-like structure, the expected relationship between the generalized variance and the scaling exponent α is:

$$\sigma_{\text{DMA}}(s) \sim s^{\alpha}. \quad (3)$$

Therefore, the log-log plot of $\sigma_{\text{DMA}}(s)$ verses s is a straight line with slope α.

2.2. Multidimensional scaling analysis using a second-Order moving polynomial function

To date, it has been reported that a high-order polynomial trend in time series may cause spurious scaling behavior, which will reduce the accuracy of the scaling exponent estimation [13,25]. Therefore, we introduce second-order moving average detrending for the scaling analysis in d-dimensional space. In addition, the algorithm of the fourth-order moving average method in 2D space is mentioned in Appendix A. For any scale n that considers odd integer values, we represent s by $s = 2m + 1$, where m is a positive integer. Similar to the central DMA in 1D space [13], we introduce a parallel translation technique to describe and implement multidimensional higher order DMA. Figure 1 shows parallel translation in 2D space, where s is 5 ($m = 2$).

Considering a d-dimensional data $f(x_1, x_2, \ldots, x_d)$, the trend estimated by the second-order polynomial function based on the least-squares fit is as follows:

$$\tilde{f}(x_1, x_2, \ldots, x_d) = a^{(0)} + \sum_{i=1}^{d} a_i^{(1)} x_i + \sum_{i=1}^{d} a_i^{(2)} x_i^2 + \sum_{i=1}^{d} \sum_{j=i+1}^{d} a_{i,j}^{(1,1)} x_i x_j. \quad (4)$$

Here, the least squares polynomial fit is performed over a region $-m \le x_i \le m$ ($i = 1, \ldots, d$). This polynomial for trend estimation is identical to the multidimensional Savitzky-Golay filter [27–29]. The coefficients $\{a^{(0)}, a_i^{(1)}, a_i^{(2)}, a_{i,j}^{(1,1)}\}$ in Eq. (4) are obtained by minimizing the square error:

$$I(\{a^{(0)}, a_i^{(1)}, a_i^{(2)}, a_{i,j}^{(1,1)}\}) = \sum_{x_1=-m}^{m} \cdots \sum_{x_d=-m}^{m} \left[f(\mathbf{x}_d) - \tilde{f}(\mathbf{x}_d) \right]^2. \quad (5)$$

To minimize Eq. (5), we calculate the partial derivative with respect to each coefficient and set all the partial derivatives to zero. Using the parallel translation technique, the value of the polynomial function at a certain data point is given by:

$$\tilde{f}(0, \ldots, 0) = a^{(0)}, \quad (6)$$

Therefore, the essential equation that provides $a^{(0)}$ is:

$$\sum_{x_1=-m}^{m} \cdots \sum_{x_d=-m}^{m} P_d^{(2)} \left(P_d^{(2)} \right)^{\mathrm{T}} \begin{pmatrix} a^{(0)} \\ a_1^{(2)} \\ a_2^{(2)} \\ \vdots \\ a_d^{(2)} \end{pmatrix} = \sum_{x_1=-m}^{m} \cdots \sum_{x_d=-m}^{m} P_d^{(2)} f(\mathbf{x}_d), \quad (7)$$

where

$$P_d^{(2)} = \begin{pmatrix} 1 \\ x_1^2 \\ x_2^2 \\ \vdots \\ x_d^2 \end{pmatrix}. \quad (8)$$

Finally, by solving Eq. (7), we obtain the general formula for the second-order moving average polynomial function in d-dimension:

$$\tilde{f}(\mathbf{x}_d) = \frac{\left\{ (5d+4)m^2 + (5d+4)m - 3 \right\} S^{(0)}(\mathbf{x}_d) - 15 \sum_{i=1}^{d} S_i^{(2)}(\mathbf{x}_d)}{(4m^2 + 4m - 3)(2m+1)^d}, \quad (9)$$

where

$$S^{(0)}(\mathbf{x}_d) = \sum_{\xi_1=-m}^{m} \cdots \sum_{\xi_d=-m}^{m} f(x_1 + \xi_1, \ldots, x_d + \xi_d) \quad (10)$$
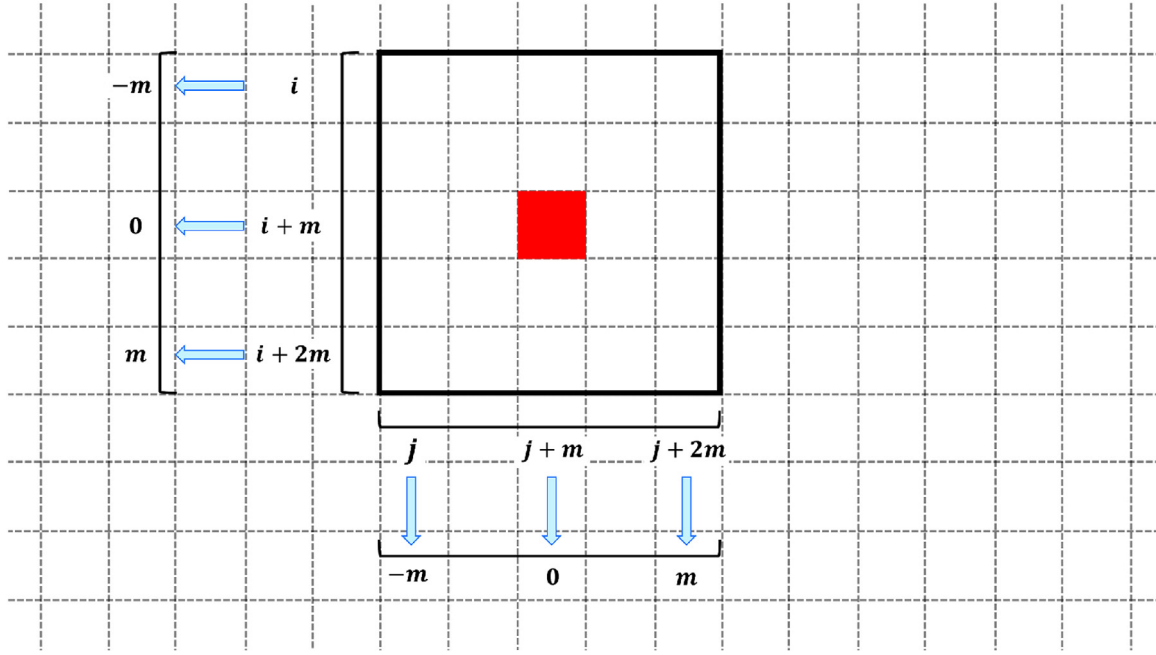
Fig. 1. Parallel translation technique for $s = 5$ ($m = 2$) in 2D space. Each square represents a data point in this 2D time series. The central point (the red square) is shifted to (0,0), which converts the calculation interval into a symmetrical interval $[-m, m]$ in each dimension. (For interpretation of the references to colour in this figure legend, the reader is referred to the web version of this article.)

$$S_i^{(2)}(\mathbf{x}_d) = \sum_{\xi_1=-m}^{m} \cdots \sum_{\xi_d=-m}^{m} \xi_i^2 f(x_1 + \xi_1, \ldots, x_d + \xi_d) \qquad (11)$$

Figure 2 shows the estimated trend of an fBm surface with Hurst exponent $H = 0.7$ and detrending results. In this study, the fBm surface was artificially generated based on the midpoint interpolation method [30,31]. Based on Eqs. (10) and (11), we analyze the time complexity of our algorithm. For example, given a 2D time series with size $S = N \times N$ and scale n, the calculation step of the summation of $f(x_1, x_2)$ in Eqs. (10) and (11) is $n^2(N - n + 1)^2$, which is proportional to N^2. With regard to the application of the scaling analysis, n is defined by a sequence $n'_1, n'_2, \ldots, n'_L$, where L is the total number of the scales and $n'_1 < n'_2 < \cdots < n'_L$. If the sequence $\{n'_l\}_{l=1}^L$ is defined by a geometric progression with a fixed common ratio and n'_L is proportional to N, the sum of $\{n'_l\}$ is proportional to S. As a result, the summation step in Eqs. (10) and (11) is proportional to N^4. Thus, the computational complexity is $O(N^4)$. This result implies that the computation time grows steeply as the number of data points increase. It is important to note that Eq. (9) is expressed in the form of convolution. As will be shown in the next section, Eq. (9) is useful for the development of the fast algorithm of multidimensional DMA.

3. Fast algorithm for second-order 2D DMA

As discussed in the aforementioned section, the calculation time of the algorithm rapidly increases when the number of data points increases. In this section, we propose a fast algorithm for second-order 2D DMA. We developed two approaches to derive the fast algorithm: First, we use the parallel translation technique to describe the algorithm, as explained in Section 2. Second, we calculate Eqs. (10) and (11) with a recurrence formula. The use of the parallel translation technique will simplify the calculation of the value of the polynomial function at a certain data point as $\tilde{f}(0, \ldots, 0) = a^{(0)}$, which implies that the calculation of other coefficients of the polynomial function is not necessary. In Eq. (9),

the calculation of $S^{(0)}$ and $S^{(2)}$ is time-consuming. Herein, we solve this problem by using the recurrence formula of $S^{(0)}$ and $S^{(2)}$. Based on Eq. (1), the generalized variance of a 2D time series $f(x_1, x_2)$ at scale n is defined as:

$$\sigma_{\text{DMA}}^2(s) = \frac{1}{(N_1 - s + 1)(N_2 - s + 1)} \sum_{x_1 = \frac{s-1}{2}}^{N_1 - \frac{s-1}{2}} \sum_{x_2 = \frac{s-1}{2}}^{N_2 - \frac{s-1}{2}} \left[f(x_1, x_2) - \tilde{f}(x_1, x_2) \right]^2.$$

$$(12)$$

Here, N_1 and N_2 are the lengths in each dimension respectively. According to Section 2, by replacing n with $2m + 1$, $\tilde{f}(x_1, x_2)$ is given by

$$\tilde{f}(x_1, x_2) = \frac{14m(m+1) - 3}{(2m+1)^2(4m(m+1) - 3)} S_m^{(0,0)}(x_1, x_2)$$
$$- \frac{15}{(2m+1)^2(4m(m+1) - 3)} S_m^{(2,0)}(x_1, x_2)$$
$$- \frac{15}{(2m+1)^2(4m(m+1) - 3)} S_m^{(0,2)}(x_1, x_2), \qquad (13)$$

where

$$S_m^{(0,0)}(x_1, x_2) = \sum_{i=-m}^{m} \sum_{j=-m}^{m} f(x_1 + i, x_2 + j), \qquad (14)$$

$$S_m^{(2,0)}(x_1, x_2) = \sum_{i=-m}^{m} \sum_{j=-m}^{m} i^2 f(x_1 + i, x_2 + j), \qquad (15)$$

$$S_m^{(0,2)}(x_1, x_2) = \sum_{i=-m}^{m} \sum_{j=-m}^{m} j^2 f(x_1 + i, x_2 + j). \qquad (16)$$

Let us consider the general forms of Eqs. (14)–(16), which is denoted by $S_m^{(k,l)}(x_1, x_2) = \sum_{i=-m}^{m} \sum_{j=-m}^{m} i^k j^l f(x_1 + i, x_2 + j)$ ($k, l = 0, 1, 2, \ldots$). In our algorithm, $S_m^{(k,l)}(x_1, x_2)$ is calculated for each point of $f(x_1, x_2)$, where $m \le x_1 \le N_1 - m$ and $m \le x_2 \le N_2 - m$. The calculation for the next point is performed by incrementing
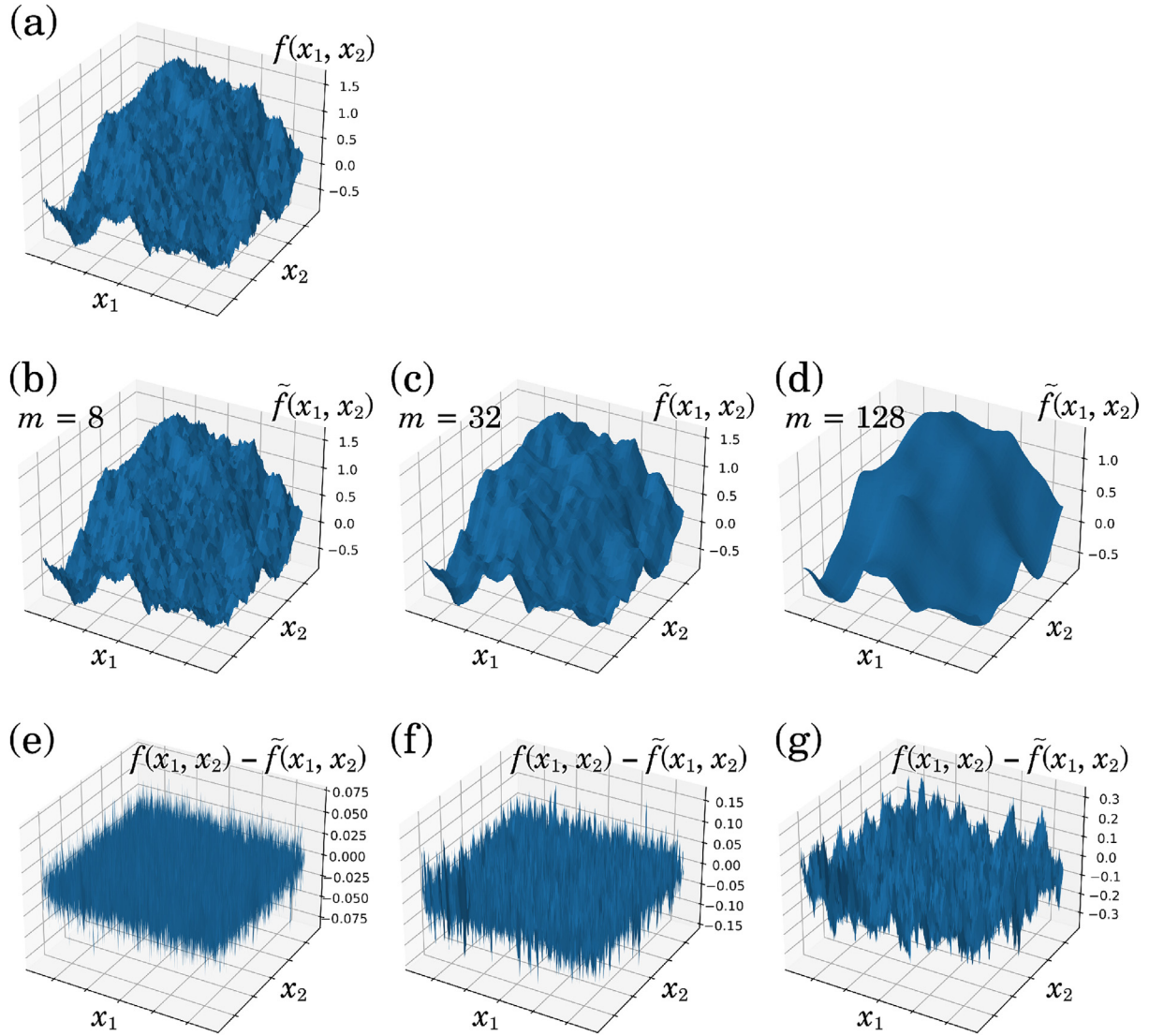
Fig. 2. Example of two-dimensional second-order DMA for the analysis of a fBm surface with $H = 0.7$. (a) The 3D view of a fBm surface $f(x_1, x_2)$ with $H = 0.7$ and a size of 1025 ×1025 pixels. (b-d) Results of the second-order moving average $\tilde{f}(x_1, x_2)$ with a scale of $n =17, 65$, and 257 ($m =8, 32$, and 128, respectively). (e-g) The detrending results $f(x_1, x_2) - \tilde{f}(x_1, x_2)$ using the moving average results shown in (b-d) respectively.

x_1 or x_2. Specifically, it defines the calculation of $S_m^{(k,l)}(x_1 + 1, x_2)$ or $S_m^{(k,l)}(x_1, x_2 + 1)$ using the recurrence formula:

$$S_m^{(k,l)}(x_1 + 1, x_2) = \sum_{h=0}^{k} \binom{k}{h}(-1)^{k-h} S_m^{(h,l)}(x_1, x_2)$$
$$+ \sum_{j=-m}^{m} j^l \Big\{ m^k f(x_1 + m + 1, x_2 + j)$$
$$- (-m - 1)^k f(x_1 - m, x_2 + j) \Big\}, \quad (17)$$

$$S_m^{(k,l)}(x_1, x_2 + 1) = \sum_{h=0}^{l} \binom{l}{h}(-1)^{l-h} S_m^{(k,h)}(x_1, x_2)$$
$$+ \sum_{i=-m}^{m} i^k \Big\{ m^l f(x_1 + i, x_2 + m + 1)$$
$$- (-m - 1)^l f(x_1 + i, x_2 - m) \Big\}. \quad (18)$$

When two different scales $s_1 = 2m_1 + 1$ and $s_2 = 2m_2 + 1$ ($m_2 > m_1$ and $\Delta m = m_2 - m_1$) are given, $S_{m_2}^{(k,l)}(x_1 + \Delta m, x_2 + \Delta m)$ can be calculated using $S_{m_1}^{(k,l)}(x_1, x_2)$ based on the recurrence formula:

$$S_{m_2}^{(k,l)}(x_1 + \Delta m, x_2 + \Delta m) = \sum_{h=0}^{k}\sum_{u=0}^{l} \binom{k}{h}\binom{l}{u}(-\Delta m)^{k+l-u-h} S_{m_1}^{(h,u)}(x_1, x_2)$$
$$+ \sum_{i=m_1+1}^{m_2+\Delta m} \sum_{j=-m_1}^{m_1} (i - \Delta m)^k (j - \Delta m)^l$$
$$f(x_1 + i, x_2 + j)$$
$$+ \sum_{i=-m_2}^{m_2} \sum_{j=m_1+1}^{m_2+\Delta m} i^k j^l f(x_1 + \Delta m + i, x_2 + j). \quad (19)$$

Therefore, Eqs. (14)–(16) can be calculated across x_1 and x_2 and scale by substituting k and l with 0 or 2 in Eqs. (17)–(19). As described in Appendix A, the fast algorithm of fourth-order 2D DMA can be derived from Eqs. (17)–(19). To evaluate the efficiency of the proposed fast algorithm, we estimate the computation time of 2D DMA. Here, for a 2D time series with size $S = N \times N$, the analyzed scales $\{n_1, n_2, \ldots, n_k\}$ are the odd integers nearest to the geometric progression with a common ratio of $2^{1/2}$ and less than $N/10$. Thus, the number of the analyzed scales is approximately proportional to $\log N$. As shown in Fig. 3, the convolution-based imple-
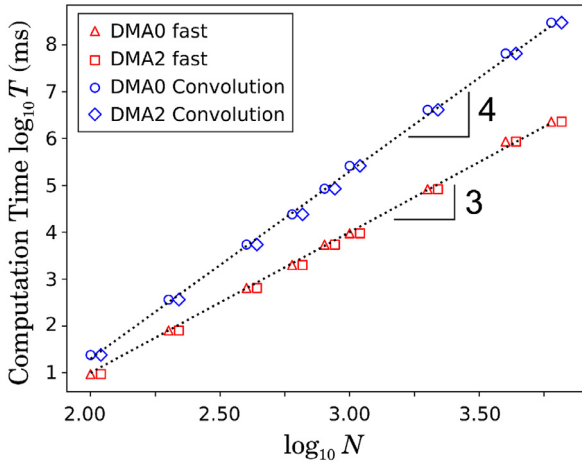
Fig. 3. Comparison of computation time. The computation time were averaged over 5 runs. The Comparison was conducted on a PC with Windows operating system and Intel(R) Core (TM) i7-8086k CPU (4.00GHz).

mentation of second-order 2D DMA incurs a much higher computational cost that is approximately proportional to N^4. In contrast, the computation time of the proposed fast algorithm is approximately proportional to N^3. Thus, the computational complexity is $O(N^3)$. DFA is one of the most widely used method. As shown in

[13], its computational complexity is comparable with that of the fast implementation algorithm of DMA.

4. Accuracy of the scaling analysis of 2D DMA

In this section, we evaluate the accuracy of the Hurst exponent estimation of 2D DMA. We conduct the experiment on fBm surfaces of different sizes (257×257, 1025×10225, and 4096×4097) with different Hurst exponent.

4.1. 2D DMA gained higher accuracy on a larger size fbm surface

For a fixed Hurst exponent, as the size of the fBm surface approaches infinity, the estimated result will converge to the true value with probability 1 according to the law of large numbers. However, as the real fBm surface exhibits a finite size, the estimation accuracy on the smaller fBm surface will be lower than that on the larger surface. Table 1 lists these results, where the estimated Hurst exponent gets closer to the true value with an increase in the data size for a fixed Hurst exponent. Figure 4(b) and (c) illustrate these results with sizes 4097×4097 and 257×257, respectively; the Hurst exponent of each fBm surface is 0.9. The black dash line represents the slop of 0.9.

We can see that the estimation on the surface with the size of 4097×4097 shows the slope much closer to 0.9 than that on the surface with the size of 257×257. Finally, Fig. 4(d) summarizes the estimation accuracy of the fBm surface with three different sizes
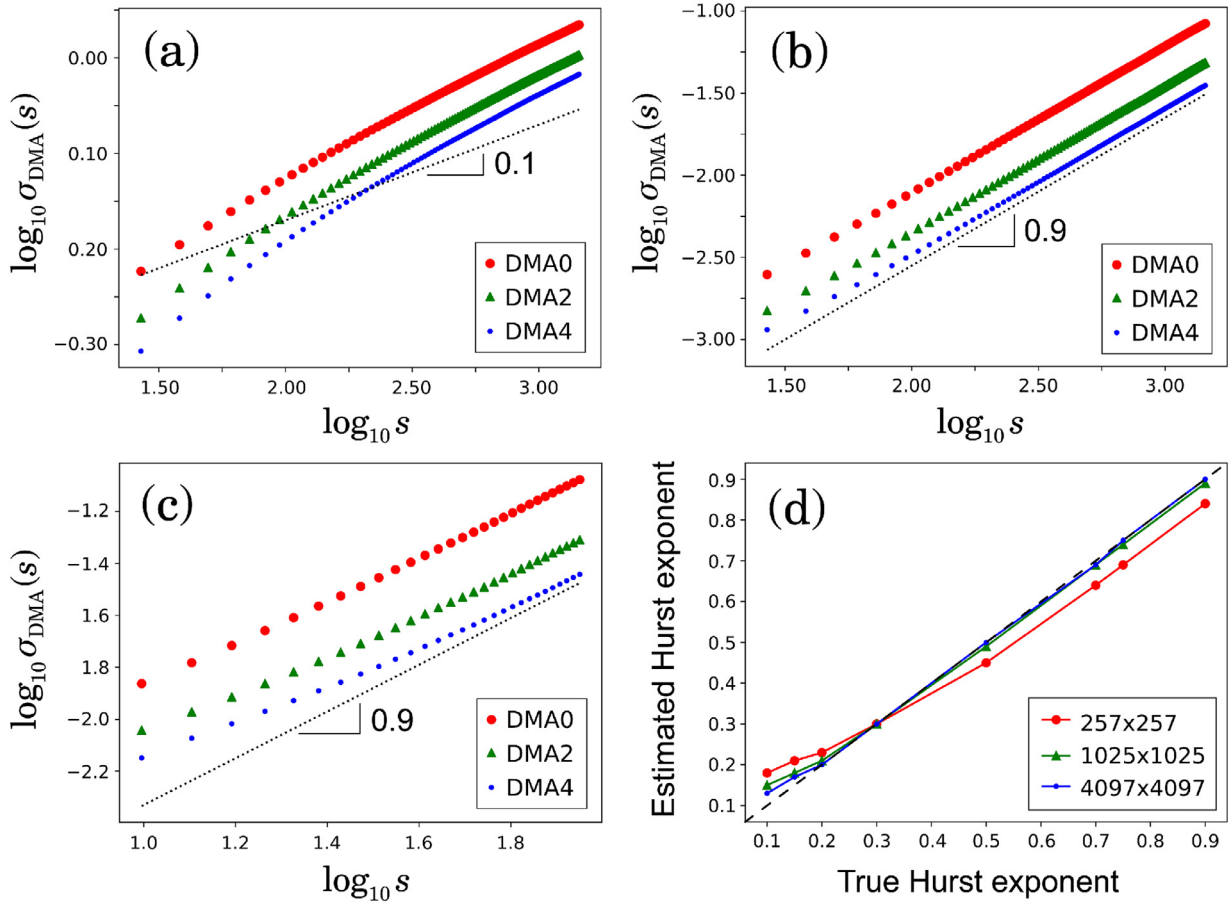

Fig. 4. Visualization of the estimation of the Hurst exponent. The result was obtained from the average of 100 samples. (a) Result of the fBm surface with a size of 4097×4097 pixels and a Hurst exponent of 0.1. The black dash line denotes the slope of 0.1. (b) Result of the fBm surface with a size of 4097×4097 pixels and a Hurst exponent of 0.9. The black dash line denotes the slope of 0.9. (c) Result of the fBm surface with a size of 257×257 pixels and a Hurst exponent of 0.9. The black dash line denotes the slope of 0.9. (d) Estimation results of the fBm surface with different sizes and different Hurst exponents.
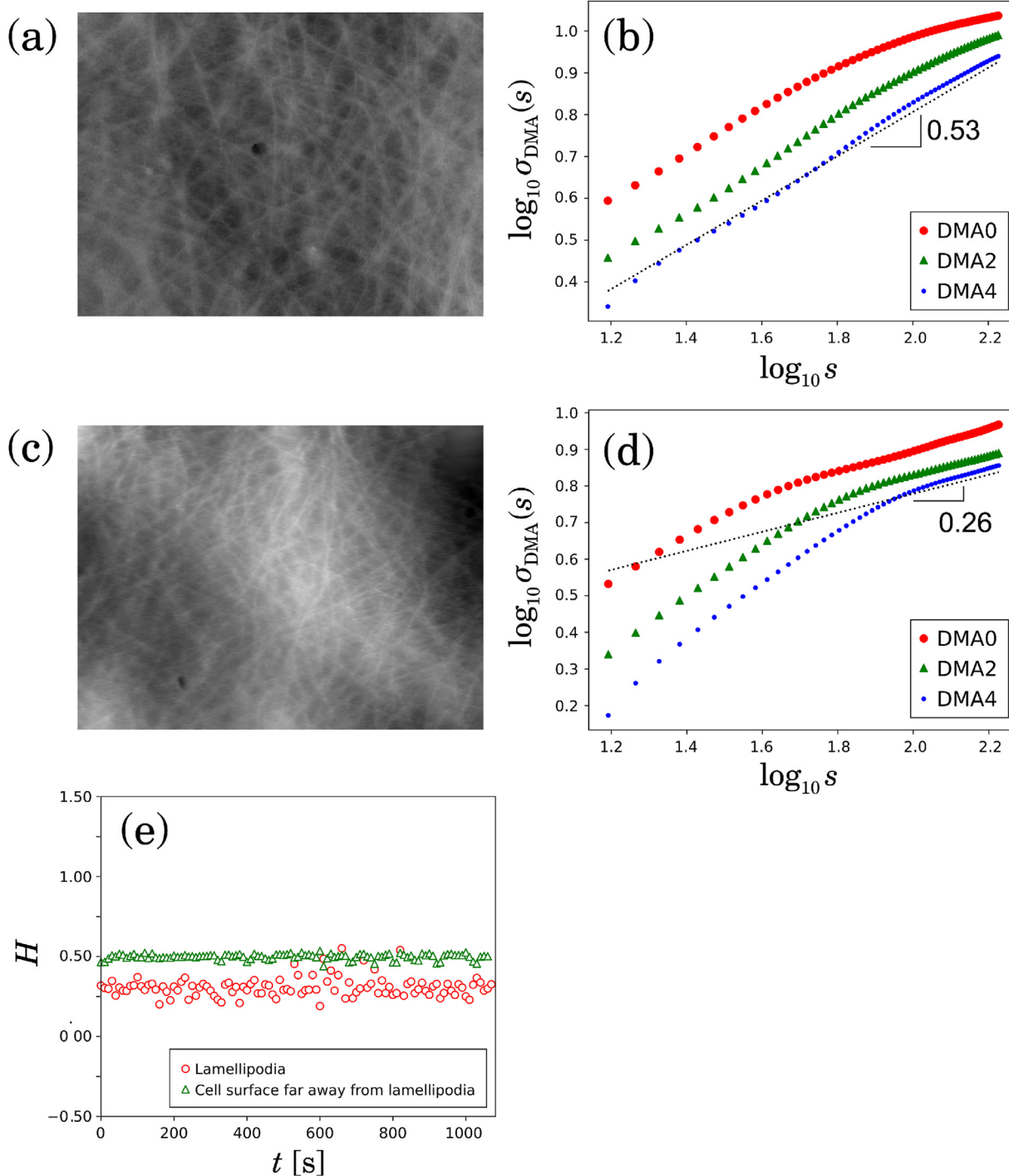
Fig. 5. (a) Actin filament network far away from lamellipodia. (b) Log-log plot of $\log_{10} s$ versus $\log_{10} \sigma_{DMA}(s)$ in (a) using zeroth-order, second-order, and fourth-order DMA. The Hurst exponent is 0.53, which is calculated using the linear regression of data points in the log-log plot. (c) Actin filament network on lamellipodia. (d) Log-log plot of $\log_{10} s$ versus $\log_{10} \sigma_{DMA}(s)$ in (c) using zeroth-order, second-order, and fourth-order DMA. The Hurst exponent is 0.26, which is calculated using the linear regression of data points in the log-log plot. (e) Change in the Hurst exponent of the actin filament network shown in (a) and (c) over time. The result suggests that the fiber density of the actin filament network far away from lamellipodia was almost constant, whereas the fiber density of the actin filament network on lamellipodia changed frequently and dramatically.

and Hurst exponents, where the black dash line implies that the estimated Hurst exponent signifies the true value.

4.2. 2D DMA gained higher accuracy on the fBm surface with a larger scaling exponent

For a fixed size, the estimation of the low Hurst exponent is less accurate than that of the high Hurst exponent. As listed in

Table 1, for the same data size, the estimation error of the fBm surface with a higher Hurst exponent is smaller than that with a lower Hurst exponent. Fig. 4(a) illustrates the Hurst exponent estimation of the fBm surface with the size of 4097 × 4097; the Hurst exponent is 0.1, which implies that the slope is larger than 0.1. Figure 4(d) shows this result as well, where we can observe that the estimation shows a larger error when the Hurst exponent is smaller than 0.2.

Table 1
The Hurst exponent estimation result using 2D DMA. The experiment was conducted on fBm surface with different size and different Hurst exponent, and each result was obtained by averaging 100 samples.

Hurst	Data	Order		
Exponent	Size	Zero Order	Second Order	Forth Order
	257×257	0.16 ± 0.02	0.18 ± 0.02	0.20 ± 0.01
$H = 0.1$	1025×1025	0.14 ± 0.02	0.15 ± 0.02	0.16 ± 0.01
	4097×4097	0.13 ± 0.01	0.13 ± 0.01	0.14 ± 0.01
	257×257	0.86 ± 0.07	0.84 ± 0.05	0.81 ± 0.03
$H = 0.9$	1025×1025	0.88 ± 0.07	0.89 ± 0.06	0.88 ± 0.05
	4097×4097	0.89 ± 0.04	0.90 ± 0.03	0.90 ± 0.03

5. Application of the multidimensional DMA

To date, the Hurst exponent was used to quantify the diversity of 3D landscape, and, thus may be extended to quantitatively describe the atomic-force-microscope (AFM) images of electrospun nanofiber mats [32,33]. In this section, we show an application of the proposed method that can be used as a tool to quantitatively describe the density of the actin filament network behind the cell cortex. We assume that the fiber network with higher fiber density will exhibit diversity with regard to the representation of its image. If an image of a fiber network has a higher Hurst exponent, the diversity of the image surface is low, which implies less content on the image and thus, the fiber density is low. Our video data were imaged by fast-scanning atomic force microscopy and represented the organization of the actin filament network dynamics behind the cell cortex in a living cell [34]. Two kinds of the actin filament network were imaged: One is the actin filament network on the cell surface far away from lamellipodia (Fig. 5(a)), and the other is the actin filament network on the cell surface of lamellipodia (Fig. 5(c)). These two images are two snapshots of two videos with an image size of 640×480 pixels, respectively. We used COS-7 cells that were derived from monkey kidney tissue. Figure 5(b) and (d) show the results of the Hurst exponent estimation of the actin filament network structure shown in Fig. 5(a) and (c). The results show the power-law scaling between $\log_{10} s$ and $\log_{10} \sigma_{\mathrm{DMA}}(s)$, where the data points are approximately located on a straight line, which suggests that the structure of the two kinds of the actin filament network behave self-similarity properties. The estimated Hurst exponents of the actin filament network on the cell surface far away from and of lamellipodia are 0.53 and 0.26, respectively, which implies that the fiber density of the latter actin filament network is higher. These Hurst exponents are obtained using the linear regression of data points in the log-log plot. It is worth noticing that the result of the estimated Hurst exponent is independent to the order of DMA, which means that the estimated scaling exponent remains unchanged when the order of DMA changes. Finally, we calculate the Hurst exponent of the actin filament network shown in the frame of each video. The change in the Hurst exponent versus time is shown in Fig. 5(e). Figure 5(e) demonstrates that the Hurst exponent of the actin filament network far away from lamellipodia rarely changed, whereas the Hurst exponent of the actin filament network on lamellipodia dramatically changed. This result reveals that during the imaging process, the fiber density of the actin filament network far away from lamellipodia stayed around a constant, whereas the fiber density of the actin filament network on lamellipodia frequently and dramatically changed. This is because the actin filament network on lamellipodia plays the role of cell migration, and the generation and degeneration of actin filament happen frequently; thus, its density changes frequently and dramatically. However, the actin filament network far away from lamellipodia does not exhibit this kind of behavior; therefore, its density almost remains constant.

6. Summary and discussion

In this study, we proposed a multidimensional higher order detrending moving average algorithm for fractal analysis in higher dimensional space; moreover, we analytically derived its formula and fast algorithm in 2D space. The experiments showed that the proposed fast algorithm can reduce the computational time compared with the conventional convolution-based implementation and revealed that the proposed method can gain higher estimation accuracy on a larger fBm surface or with a higher Hurst exponent. Moreover, we demonstrate the application of the proposed method as a tool to quantitatively describe the density of the actin filament network behind the cell cortex. According to the previous study, higher dimensional DFA was widely applied to image analysis [35–37], whereas higher dimensional DMA [23] was rarely used. Thus, our study can facilitate the application of higher order DMA to various investigations, e.g., the multifractal [22] and scaling analysis of time series in higher dimensional space.

Declaration of Competing Interest

The authors declare the following financial interests/personal relationships which may be considered as potential competing interests:

Ken Kiyono reports financial support was provided by Japan Society for the Promotion of Science.

CRediT authorship contribution statement

Hanqiu Ju: Writing – original draft, Software, Investigation. **Naoki Honda:** Investigation, Writing – review & editing. **Shige H. Yoshimura:** Investigation, Resources, Data curation. **Miki Kaneko:** Investigation, Writing – review & editing. **Taiki Shigematsu:** Investigation, Writing – review & editing. **Ken Kiyono:** Conceptualization, Writing – review & editing, Methodology, Software, Supervision, Funding acquisition.

Data availability

Data will be made available on request.

Appendix A. 2D DMA using the fourth-order moving polynomial function

In the case of 2D DMA, using the fourth-order moving polynomial function, the fourth-order polynomial trend can be defined as:

$$
\begin{aligned}
\tilde{f}(x_1, x_2) = & \, a^{(0)} + a_1^{(1)} x_1 + a_2^{(1)} x_2 + a_1^{(2)} x_1^2 + a_2^{(2)} x_2^2 + a_{1,2}^{(1,1)} x_1 x_2 \\
& + a_1^{(3)} x_1^3 + a_2^{(3)} x_2^3 + a_{1,2}^{(2,1)} x_1^2 x_2 + a_{1,2}^{(1,2)} x_1 x_2^2 \\
& + a_1^{(4)} x_1^4 + a_2^{(4)} x_2^4 + a_{1,2}^{(2,2)} x_1^2 x_2^2 + a_{1,2}^{(3,1)} x_1^3 x_2 \\
& + a_{1,2}^{(1,3)} x_1 x_2^3 .
\end{aligned}
\tag{A1}
$$

Similar coefficients of Eq. (5) can be obtained by minimizing the loss function

$$
I(\{\mathbf{a}\}) = \sum_{x_1=-m}^{m} \sum_{x_2=-m}^{m} \left[f(x_1, x_2) - \tilde{f}(x_1, x_2) \right]^2 .
\tag{A2}
$$

Here, **a** is a vector that contains all the coefficients of Eq. (A1). By setting the derivative of Eq. (A2) with respect to **a** to zero, we can obtain the essential equation that provides $a^{(0)}$:

$$\sum_{x_1=-m}^{m} \cdots \sum_{x_d=-m}^{m} P_d^{(4)} \left(P_d^{(4)}\right)^{\mathrm{T}} \begin{pmatrix} a^{(0)} \\ a_1^{(2)} \\ a_2^{(2)} \\ a_1^{(4)} \\ a_2^{(4)} \\ a_{1,2}^{(2,2)} \end{pmatrix} = \sum_{x_1=-m}^{m} \cdots \sum_{x_d=-m}^{m} P_d^{(4)} f(x_1, x_2),$$

(A3)

where

$$P_d^{(4)} = \begin{pmatrix} 1 \\ x_1^2 \\ x_2^2 \\ x_1^4 \\ x_2^4 \\ x_1^2 x_2^2 \end{pmatrix}.$$

(A4)

By solving Eq. (A3), we can obtain the formula of the fourth-order moving average polynomial function:

$$\begin{aligned} \tilde{f}(x_1, x_2) = & \Big[\big(1944m^6 + 5832m^5 - 1674m^4 - 13068m^3 - 3150m^2 \\ & + 4356m - 540\big) S_m^{(0,0)}(x_1, x_2) \\ & - \big(5400m^4 + 10800m^3 - 8550m^2 - 13950m + 4725\big) \\ & \big(S_m^{(2,0)}(x_1, x_2) + S_m^{(0,2)}(x_1, x_2)\big) \\ & + 945\big(4m^2 + 4m - 3\big)\big(S_m^{(4,0)}(x_1, x_2) + S_m^{(0,4)}(x_1, x_2)\big) \\ & + 900\big(4m^2 + 4m - 15\big)S_m^{(2,2)}(x_1, x_2) \Big]/D, \end{aligned}$$

(A5)

where

$$D = 4\big(4m^2 + 4m - 15\big)\big(8m^3 + 12m^2 - 2m - 3\big)^2.$$

(A6)

The fast algorithm for Eq. (A6) that calculates across x_1 and x_2 and scale can be obtained from Eqs. (17)–(19).

Appendix B. Detrending capability of 2D DMA

One advantage of higher order DMA is its improved detrending performance, which plays a vital role in improving the estimation accuracy of the scaling exponent. To show this, we analyzed the 2D data array generated by the superposition of the fBm surface with Hurst exponent H=0.7 and the higher order polynomial trend (Fig. 6).

As shown in Fig. 7, we analyzed the fBm surface with the superposition of second-, fourth-, fifth-, and sixth-order polynomial trends. The plot shows spurious scaling behavior at a large scale, as suggested by the slope much steeper than 0.7 at a large value of s. The steep slope is caused by the adverse effect of the deterministic higher order two-dimensional polynomial pattern. However, the result illustrated in Fig. 7 suggests that as the order of DMA increases, the spurious scaling behavior will be attenuated or even disappear. For example, spurious scaling behavior has not occurred in fourth-order DMA while analyzing time series with second-, fourth-, and fifth-order trends; it occurs at the zeroth-order DMA. Moreover, this numerical study shows that mth order 2D DMA can accurately perform the scaling analysis of a fBm surface with the $m + 1$ order trend, which coincides with the result of 1D DMA [13,25].

Here, we analytically show that the second-order 2D DMA can remove deterministic patterns described by the cubic polynomial surface. When we consider the summation of two uncorrelated data $f^A(x, y)$ and $f^B(x, y)$, the superposition law of the mean square deviation in DMA holds [38]:

$$\left(\sigma_{\mathrm{DMA}}^{(A+B)}(s)\right)^2 = \left(\sigma_{\mathrm{DMA}}^{(A)}(s)\right)^2 + \left(\sigma_{\mathrm{DMA}}^{(B)}(s)\right)^2,$$

(B1)

where $\sigma_{DMA}^{(A+B)}(s)$, $\sigma_{DMA}^{(A)}(s)$ and $\sigma_{DMA}^{(B)}(s)$ denote the root-mean-square deviation corresponding to $\{f^A(x, y) + f^B(x, y)\}$, $\{f^A(x, y)\}$, and $\{f^B(x, y)\}$, respectively. Therefore, if a data array is defined by the summation of a stochastic pattern and a polynomial surface, the additive law of mean-square deviations holds. Therefore, we can study the separate effects of the polynomial surface. To simplify the calculation, we assume a cubic polynomial surface $S^3(x, y)$ defined in the region $-m \le x \le m$, $-m \le y \le m$, where the scale is given by $s = (2m+1)^2$:

$$\begin{aligned} S^3(x, y) = & c_{0,0} + c_{1,0}x + c_{0,1}y + c_{2,0}x^2 + c_{0,2}y^2 + c_{3,0}x^3 + c_{2,1}x^2 y \\ & + c_{1,2}xy^2 + c_{0,3}y^3. \end{aligned}$$

(B2)

By employing parallel translation, an arbitrary situation while analyzing the cubic polynomial surface can be described in the aforementioned form. To calculate $\tilde{f}^2(x, y)$ at $(x, y) = (0, 0)$ on the moving polynomial surface, we obtain the coefficients $\{a_{i,j}\}$ of the least-square polynomial surface by minimizing

$$I\big(\{a_{i,j}\}\big) = \sum_{x_1=-m}^{m} \sum_{y=-m}^{m} \big(S^{(3)}(x_1, x_2) - \tilde{f}^2(x, y)\big)^2.$$

(B3)

where

$$\tilde{f}^2(x, y) = a_{0,0} + a_{1,0}x + a_{0,1}y + a_{2,0}x^2 + a_{1,1}xy + a_{0,2}y^2.$$

(B4)

(a) fBm surface   (b) Second-order polynomial trend   (c) fBm surface with trend
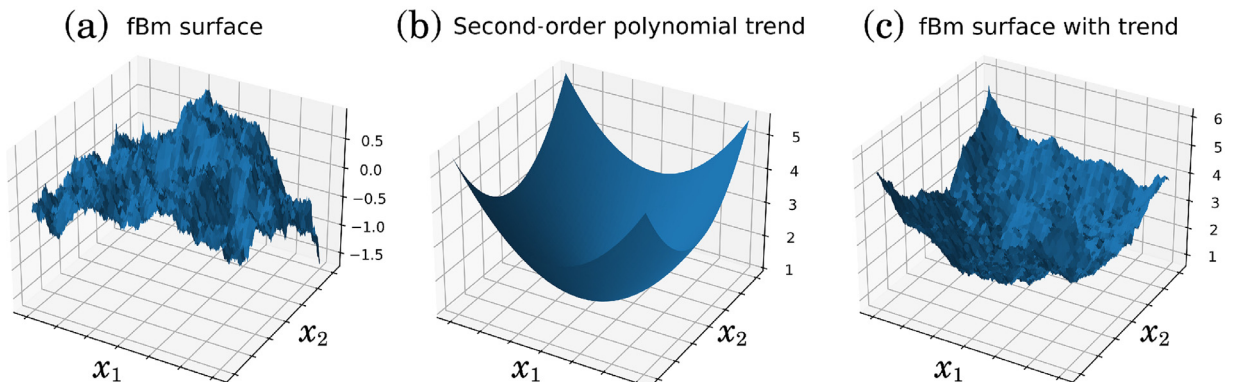

Fig. 6. (a) fBm surface with a size of 1025 × 1025 pixels and H=0.7. (b) 2D polynomial trend. (c) The superposition of the fBm surface and the second-order polynomial trend are shown in (a) and (b), respectively.
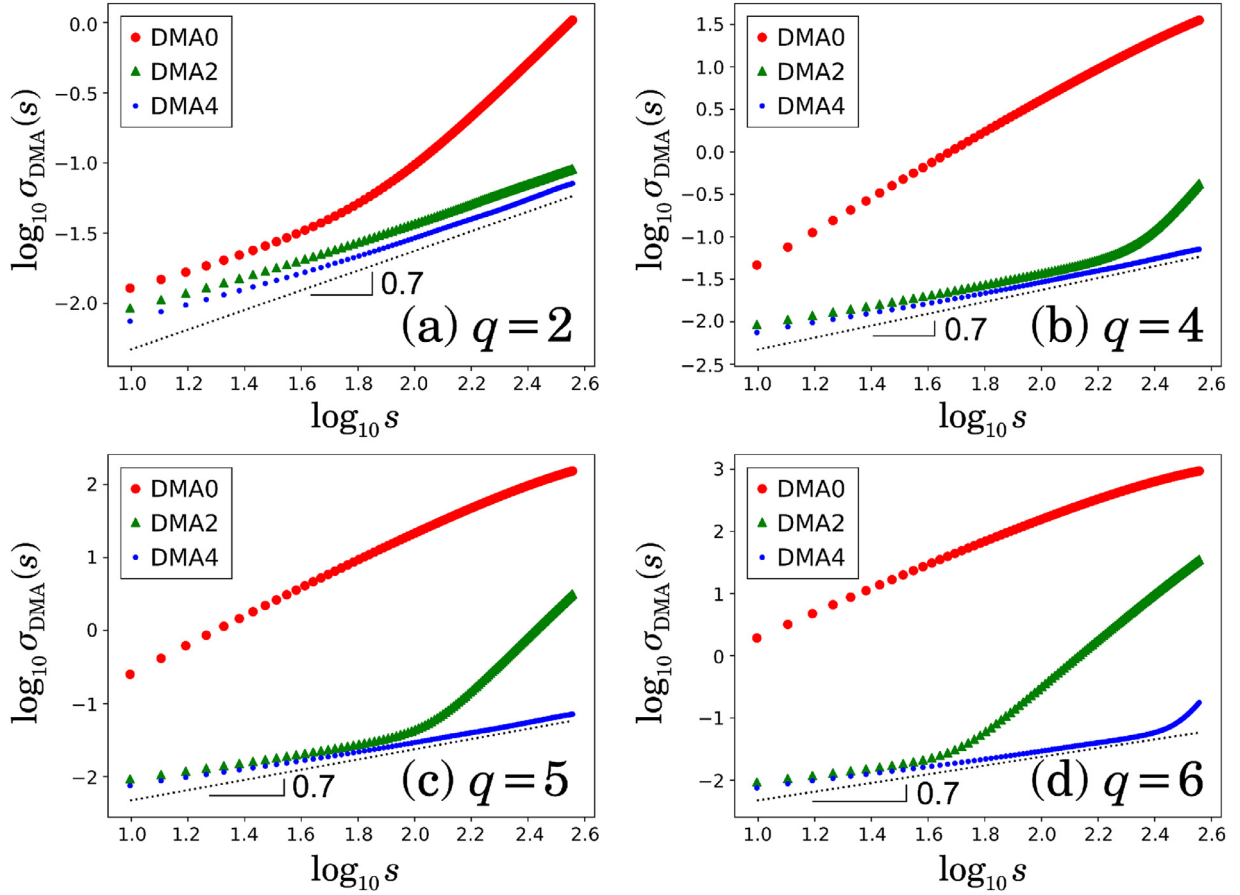
Fig. 7. Results of the detrending capability of 2D mth-order DMA. (a, b, c, and d) are the estimation results of the fBm surface (H is 0.7 and size is 1025×1025 pixels). q is the order of the polynomial trend. The results are obtained by averaging 100 samples. The black dashed line denotes the slope of 0.7.

Thus, we solve the following equations:

$$\frac{\partial I(\{a_{i,j}\})}{\partial a_{k,l}}. \tag{B5}$$

Equation defined by Eq. (B4) for a pair of even numbers of i and j results in

$$\sum_{x=-m}^{m} \sum_{y=-m}^{m} \begin{bmatrix} 1 & x^2 & y^2 \\ x^2 & x^4 & x^2y^2 \\ y^2 & x^2y^2 & y^4 \end{bmatrix} \begin{bmatrix} c_{0,0} - a_{0,0} \\ c_{2,0} - a_{2,0} \\ c_{0,2} - a_{0,2} \end{bmatrix} = \begin{bmatrix} 0 \\ 0 \\ 0 \end{bmatrix}. \tag{B6}$$

AS m is a positive integer, the matrix in Eq. (B6) is regular. Thus, we can obtain

$$a_{0,0} = c_{0,0}$$
$$a_{2,0} = c_{2,0}$$
$$a_{0,2} = c_{0,2} \tag{B7}$$

In this case, the moving average point at $(x, y) = (0, 0)$ on the polynomial surface $\tilde{f}^{(2)}(x, y)$ is given by

$$\tilde{f}^{(2)}(0, 0) = a_{0,0} = c_{0,0}. \tag{B8}$$

Therefore, the square deviation based on the cubic polynomial surface $S^{(3)}(x, y)$ is calculated as

$$\left(S^{(3)}(x, y) - \tilde{f}^{(2)}(x, y)\right)^2 \Big|_{x=0, y=0} = (c_{0,0} - a_{0,0})^2 = 0, \tag{B9}$$

This result demonstrates that $\sigma_{\text{DMA}}^2(s) = 0$ when a polynomial surface with degree $q \leq 3$ is analyzed by second-order 2D DMA.

In contrast, it is possible to demonstrate that zeroth-order 2D DMA can remove flat surface patterns described by $S^{(1)}(x, y) = c_{0,0} + c_{0,0}x + c_{0,1}y$. Furthermore, when a quadratic polynomial surface (elliptical paraboloid), $S^{(2)}(x, y) = S^{(1)}(x, y) + c_{2,0}x^2 + c_{1,1}xy + c_{0,2}y^2$, is analyzed using zeroth-order 2D DMA, we obtain

$$\sigma_{\text{DMA}}^2(s) = \frac{(c_{2,0} + c_{0,2})^2}{144}(s - 1)^2, \tag{B10}$$

where $s = (2m+1)^2$. Therefore, as shown in Fig. 7(a), the spurious scaling behavior with a steeper slope is observed.

Appendix C. Limitation of the detectable scaling exponent

As reported in the study of the one-dimensional higher order DMA, the limitation of the detectable scaling exponent exists and depends on the order of DMA [13,25]. In 1D mth order DMA, the upper limit of the detectable scale of the artificially generated time series with a power-law power spectral density $S(f) \sim f^{-\beta}$ (f is the frequency) is given by $m + 2$ [25]. By conducting numerical experiments, we show that higher order 2D DMA has this limitation as well. As shown in Fig. 8, the result that has been obtained by the average of 100 generated samples suggests that the limitation of the detectable scaling exponent is determined by the order of DMA. The largest scaling exponents, which zeroth-, second-, and fourth-order DMA can detect, are 2, 4, and 6, respectively. This result suggests that the upper limit of the detectable scale is $m + 2$, and this limited detection ability is identical to 1D DMA.
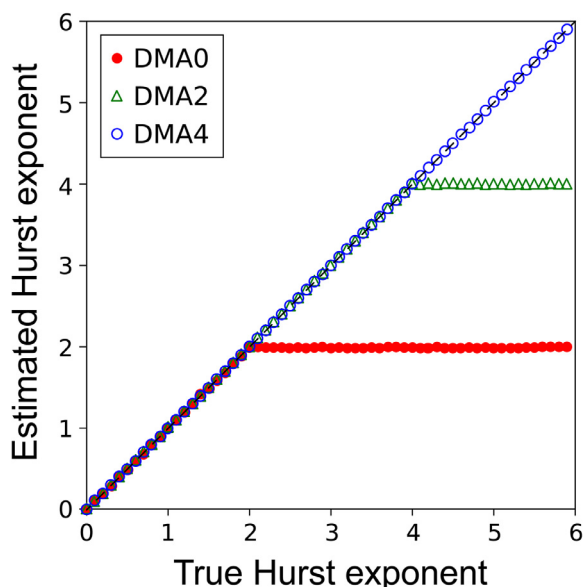
Fig. 8. The plot of the relationship between the true scaling exponent and the estimated scaling exponent using 2D zeroth-order, second-order, and fourth-order DMA. The black dash line implies that the estimated Hurst exponent signifies the true value. The results are obtained by averaging 100 samples with a size of 1025 × 1025 pixels.

References

[1] M. Kobayashi, T. Musha, 1/F fluctuation of heartbeat period, IEEE Trans. Biomed. Eng. 6 (1982) 456–457.

[2] C.-K. Peng, S.V. Buldyrev, S. Havlin, M. Simons, H.E. Stanley, A.L. Goldberger, Mosaic organization of dna nucleotides, Phys. Rev. E 49 (2) (1994) 1685.

[3] C.-K. Peng, S. Havlin, H.E. Stanley, A.L. Goldberger, Quantification of scaling exponents and crossover phenomena in nonstationary heartbeat time series, Chaos 5 (1) (1995) 82–87.

[4] K. Kiyono, Z.R. Struzik, N. Aoyagi, F. Togo, Y. Yamamoto, Phase transition in a healthy human heart rate, Phys. Rev. Lett. 95 (2005) 058101, doi:10.1103/PhysRevLett.95.058101.

[5] R.N. Mantegna, H.E. Stanley, Introduction to Econophysics: Correlations and Complexity in Finance, Cambridge university press, 1999.

[6] J. Alvarez-Ramirez, E. Rodriguez, J.C. Echeverría, Detrending fluctuation analysis based on moving average filtering, Physica A 354 (2005) 199–219.

[7] Y. Wang, Y. Wei, C. Wu, Detrended fluctuation analysis on spot and futures markets of west texas intermediate crude oil, Physica A 390 (5) (2011) 864–875.

[8] D. Rybski, S.V. Buldyrev, S. Havlin, F. Liljeros, H.A. Makse, Scaling laws of human interaction activity, Proc. Natl. Acad. Sci. 106 (31) (2009) 12640–12645.

[9] C. Fan, J.-L. Guo, Y.L. Zha, Fractal analysis on human dynamics of library loans, Physica A 391 (24) (2012) 6617–6625.

[10] B.B. Mandelbrot, J.W.V. Ness, Fractional Brownian motions, fractional noises and applications, SIAM Rev. 10 (4) (1968) 422–437.

[11] T. Nakamura, K. Kiyono, H. Wendt, P. Abry, Y. Yamamoto, Multiscale analysis of intensive longitudinal biomedical signals and its clinical applications, Proc. IEEE 104 (2) (2016) 242–261.

[12] R. Sassi, S. Cerutti, F. Lombardi, M. Malik, H.V. Huikuri, C.-K. Peng, G. Schmidt, Y. Yamamoto, D. Reviewers, B. Gorenek, et al., Advances in heart rate variability signal analysis: joint position statement by the e-cardiology ESC working group and the European heart rhythm association co-endorsed by the Asia pacific heart rhythm society, Ep Europace 17 (9) (2015) 1341–1353.

[13] Y. Tsujimoto, Y. Miki, S. Shimatani, K. Kiyono, Fast algorithm for scaling analysis with higher-order detrending moving average method, Phys. Rev. E 93 (5) (2016) 053304.

[14] L. Ponson, D. Bonamy, E. Bouchaud, Two-dimensional scaling properties of experimental fracture surfaces, Phys. Rev. Lett. 96 (3) (2006) 035506.

[15] J. Schmittbuhl, F. Renard, J.-P. Gratier, R. Toussaint, Roughness of stylolites: implications of 3D high resolution topography measurements, Phys. Rev. Lett. 93 (23) (2004) 238501.

[16] G. Rangarajan, M. Ding, Integrated approach to the assessment of long range correlation in time series data, Phys. Rev. E 61 (5) (2000) 4991.

[17] Q. Wang, W. Zhao, Z. Liang, X. Wang, T. Zhou, Y. Wu, L. Jiao, Investigation of diamond wheel topography in elliptical ultrasonic assisted grinding (EUAG) of monocrystal sapphire using fractal analysis method, Ultrasonics 84 (2018) 87–95.

[18] M. Holschneider, On the wavelet transformation of fractal objects, J. Stat. Phys. 50 (5–6) (1988) 963–993.

[19] D. Veitch, P. Abry, A wavelet-based joint estimator of the parameters of long-range dependence, IEEE Trans. Inf. Theory 45 (3) (1999) 878–897.

[20] A. Arneodo, N. Decoster, S. Roux, A wavelet-based method for multifractal image analysis. I. Methodology and test applications on isotropic and anisotropic random rough surfaces, Eur. Phys. J. B 15 (3) (2000) 567–600.

[21] G. Li, K. Zhang, J. Gong, X. Jin, Calculation method for fractal characteristics of machining topography surface based on wavelet transform, Procedia CIRP 79 (2019) 500–504.

[22] G.-F. Gu, W.X. Zhou, Detrended fluctuation analysis for fractals and multifractals in higher dimensions, Phys. Rev. E 74 (6) (2006) 061104.

[23] A. Carbone, Algorithm to estimate the hurst exponent of high-dimensional fractals, Phys. Rev. E 76 (5) (2007) 056703.

[24] S. Arianos, A. Carbone, C. Türk, Self-similarity of higher-order moving averages, Phys. Rev. E 84 (4) (2011) 046113.

[25] A. Carbone, K. Kiyono, Detrending moving average algorithm: frequency response and scaling performances, Phys. Rev. E 93 (6) (2016) 063309.

[26] K. Kiyono, Y. Tsujimoto, Nonlinear filtering properties of detrended fluctuation analysis, Physica A 462 (2016) 807–815.

[27] J.E. Kuo, H. Wang, S. Pickup, Multidimensional least-squares smoothing using orthogonal polynomials, Anal. Chem. 63 (6) (1991) 630–635.

[28] D.J. Thornley, Novel anisotropic multidimensional convolutional filters for derivative estimation and reconstruction, in: 2007 IEEE International Conference on Signal Processing and Communications, IEEE, 2007, pp. 253–256.

[29] C. Shekhar, On simplified application of multidimensional Savitzky-Golay filters and differentiators, in: AIP Conference Proceedings, Vol. 1705, AIP Publishing LLC, 2016, p. 020014.

[30] A. Fournier, D. Fussell, L. Carpenter, Computer rendering of stochastic models, Commun. ACM 25 (6) (1982) 371–384.

[31] R.F. Voss, Random fractal forgeries, in: Fundamental Algorithms for Computer Graphics, Springer, 1985, pp. 805–835.

[32] T. Blachowicz, A. Ehrmann, K. Domino, Statistical analysis of digital images of periodic fibrous structures using generalized hurst exponent distributions, Physica A 452 (2016) 167–177.

[33] T. Blachowicz, K. Domino, M. Koruszowic, J. Grzybowski, T. Böhm, A. Ehrmann, Statistical analysis of nanofiber mat AFM images by gray-scale-resolved hurst exponent distributions, Appl. Sci. 11 (5) (2021) 2436.

[34] Y. Zhang, A. Yoshida, N. Sakai, Y. Uekusa, M. Kumeta, S.H. Yoshimura, In vivo dynamics of the cortical actin network revealed by fast-scanning atomic force microscopy, Microscopy 66 (4) (2017) 272–282.

[35] J. Wang, W. Shao, J. Kim, Combining MF-DFA and LSSVM for retina images classification, Biomed. Signal Process. Control 60 (2020) 101943.

[36] F. Wang, L. Wang, R.B. Zou, Multifractal detrended moving average analysis for texture representation, Chaos 24 (3) (2014) 033127.

[37] F. Wang, Z.-S. Li, G.P. Liao, Multifractal detrended fluctuation analysis for image texture feature representation, Int. J. Pattern Recognit. Artif. Intell. 28 (03) (2014) 1455005.

[38] Y.-H. Shao, G.-F. Gu, Z.-Q. Jiang, W.X. Zhou, Effects of polynomial trends on detrending moving average analysis, Fractals 23 (03) (2015) 1550034.